crystals

MDPI

Article

Low Temperature Synthesis of Ag_2MoO_4/BiOCl Heterojunctions with Oxygen Vacancies for Improved Pollutant Degradation

Shuai Fu [1,2,*], Wanyu Pu [1], Qiang Huang [1,2], Huijie Zhu [1,2,*], Junhong Bie [3], Qi Liu [1,2], Bei Zang [1], Zhixi Zhao [4], Ying Wang [5] and Hongqiang Wang [6]

1 Henan Key Laboratory of Green Building Materials Manufacturing and Intelligent Equipment, School of Intelligent Construction and Civil Engineering, Luoyang Institute of Science and Technology, Luoyang 471023, China
2 Henan Engineering Research Center of Water Quality Safety in the Middle-Lower Yellow River, Henan Green Technology Innovation Demonstration Base, Luoyang 471023, China
3 School of Environmental Science, Liaoning University, Shenyang 110036, China
4 College of Chemistry and Chemical Engineering, Xinjiang Normal University, Urumqi 830000, China
5 School of Ecology and Environment, Ningxia University, Yinchuan 750021, China
6 School of Resource & Environment and Safety Engineering, University of South China, Hengyang 421001, China
* Correspondence: fushuai@lit.edu.cn (S.F.); huijiezhu@lit.edu.cn (H.Z.)

Abstract

The Z-scheme Ag_2MoO_4/BiOCl heterojunction with oxygen vacancies was successfully fabricated at a low temperature via a simple in situ precipitation method. The morphological, structural, and optical characteristics of the Ag_2MoO_4/BiOCl heterojunction were systematically examined. The optimized synthesized Ag_2MoO_4/BiOCl heterojunction achieved a removal rate of 80.44% for ciprofloxacin within 180 min of simulated solar irradiation, which was 3.27 and 1.90 times higher than that of pure Ag_2MoO_4 and BiOCl, respectively. The fabricated Z-scheme heterojunction and oxygen vacancies optimize the electron transfer route, enhancing the separation efficiency of photogenerated electrons and holes. Moreover, the active species trapping experiments and ESR analyses demonstrated that holes were the primary reactive species involved in the photocatalytic process. It was hypothesized that the Ag_2MoO_4/BiOCl heterojunction adhered to a Z-scheme mechanism for charge transfer. The straightforward approach opened up novel avenues for the synthesis of efficient BiOCl-based photocatalysts aimed at environmental remediation.

Keywords: Ag_2MoO_4/BiOCl; Z-scheme; oxygen vacancies; heterojunction; degradation

Check for updates

Academic Editor: Ferdinando Costantino

Received: 5 May 2026
Revised: 26 June 2026
Accepted: 30 June 2026
Published: 4 July 2026

Copyright: © 2026 by the authors. Licensee MDPI, Basel, Switzerland. This article is an open access article distributed under the terms and conditions of the Creative Commons Attribution (CC BY) license.

1. Introduction

Ciprofloxacin (CIP), a typical fluoroquinolone antibiotic, exhibits broad-spectrum antibacterial activity by inhibiting key bacterial enzymes, thereby demonstrating strong bactericidal effects against various bacteria including *Escherichia coli* and *Pseudomonas aeruginosa* [1,2]. In recent years, however, high concentrations of antibiotic pollutants have been detected, causing serious harm to natural ecosystems [3–5]. Therefore, developing a simple and efficient method to remove CIP from aquatic environments is of great significance. Various conventional treatment techniques have been proposed for eliminating organic pollutants from wastewater, including advanced oxidation processes [6], biological degradation [7], as well as electrochemical and photoelectron-Fenton reactions [8,9]. Nevertheless, most of these approaches generate undesirable by-products and require the use of unstable oxidizing agents. Within the field of advanced oxidation processes,

semiconductor-mediated photocatalysis has gained recognition as a highly promising technology due to its outstanding efficiency and chemical-free operational nature [10–15].

Bismuth oxychloride (BiOCl) is a bismuth-based semiconductor material featuring a unique layered structure, an appropriate band gap width, and excellent photocatalytic performance, making it widely applied in photocatalysis [16–19]. BiOCl possesses a layered architecture composed of alternating $[Bi_2O_2]^{2+}$ layers interconnected by double Cl^- ions via van der Waals forces. The internal electrostatic field generated by this layered structure facilitates carrier separation and enhances photocatalytic activity [20,21]. However, single-phase BiOCl suffers from low photocatalytic efficiency, which is attributable to its high recombination rate, a wide band gap, and inefficient sunlight utilization. To overcome these limitations, numerous strategies have been employed to modify the intrinsic properties of BiOCl for improved efficiency, including metal/non-metal doping [22], morphological design [23], physical structure modification, and the construction of heterostructures with other semiconductors [24–26]. Among these approaches, constructing heterojunctions has proven to be a highly effective strategy, as it can broaden the photo-responsive range and boost charge separation efficiency. For example, Chen prepared a BiOCl/TiO_2/Zn-In-modified Mg-Al LDHs composite photocatalyst (MAZB) via a one-pot steam-assisted method. The results showed that under simulated sunlight irradiation, MAZB achieved 97.5% degradation of 20 mg/L methylene blue within 120 min, with an apparent rate constant of 0.0297 min^{-1}, which was 7.2, 2.4, and 2.9 times higher than that of pristine MA, MAZ, and MAB, respectively. This was attributed to the Zn-In ion exchange effectively expanding the interlayer spacing of LDHs, the in situ growth of TiO_2 and BiOCl forming tight heterojunctions, and the one-pot steam-assisted strategy enabling uniform dispersion of active components and strong interfacial bonding, thereby promoting efficient separation of photogenerated charge carriers [27].

Due to their distinctive crystal structures, Ag-based semiconductors have emerged as promising candidate materials for photocatalytic technology. Silver molybdate (Ag_2MoO_4), a representative Ag-based material, has attracted considerable attention because of its ability to release lattice oxygen in a controllable manner, which leads to the generation of substantial reactive oxygen species (ROS) [28–30]. Ag_2MoO_4 is a white solid with a tetrahedral ionic structure, stable properties, and good visible-light response, and it has been widely used in environmental purification [31,32]. However, the poor conductivity of Ag_2MoO_4 limits charge transfer efficiency, resulting in a high recombination rate of photogenerated electron–hole pairs, thereby restricting its photocatalytic performance. The photocatalytic performance of such materials can be further improved through defect engineering, heterojunction construction, and doping modification strategies, expanding their applications in environmental remediation [33–37]. Wang first prepared a novel S-scheme $Ag_2MoO_4/ZnWO_4$ heterojunction via a coprecipitation method. Experimental results indicated that the composite prepared with a molar ratio of Mo to Zn of 3:10 exhibited the best photocatalytic activity. After 60 min of illumination the degradation efficiency of levofloxacin reached 67.0%, and the apparent first-order reaction rate constant was 0.0146 min^{-1}, which was 3.22 and 3.88 times those of pure $ZnWO_4$ and pure Ag_2MoO_4, respectively [38]. The enhanced performance is attributed to an intrinsic electric field within the heterojunction that drives directional migration of charge carriers.

In this paper, the Ag_2MoO_4/BiOCl heterojunction was prepared by a simple in situ precipitation method, and its degradation performance toward pollutants in wastewater was investigated. The effects of CIP concentration, pH, and impurity ions on CIP degradation were studied. Additionally, the degradation activity of the Ag_2MoO_4/BiOCl heterojunction toward five other pollutants (RhB, LR5B, MO, TC, and ST) in water was also explored.

2. Experimental

2.1. Chemicals

Bismuth nitrate pentahydrate ($Bi(NO_3)_3{\cdot}5H_2O$), silver nitrate ($AgNO_3$), sodium molybdate dihydrate ($Na_2MoO_4{\cdot}2H_2O$), sodium chloride (NaCl), and ethylene glycol ($(CH_2OH)_2$) were obtained from Sinopharm Chemical Reagent (Shanghai, China). All reagents were of analytical grade (AR), and deionized water was employed throughout all experimental procedures.

2.2. Synthesis of BiOCl with Oxygen Vacancies

Oxygen-vacancy-containing BiOCl was prepared following a previously reported procedure [39]. In a typical synthesis, 3 mmol of $Bi(NO_3)_3{\cdot}5H_2O$ was dissolved in 45 mL of ethylene glycol to form solution A. Subsequently, 6 mmol of NaCl was dissolved in 25 mL of deionized water, and the resulting solution was added dropwise into solution A. The obtained mixture was magnetically stirred for 3 h at 90 °C under water-bath conditions. The resulting product was collected by centrifugation, washed several times with deionized water and ethanol, and then dried at 80 °C for 24 h; this sample was designated as BiOCl-OVs. Pristine BiOCl was synthesized via a similar procedure except that no ethylene glycol was added.

2.3. Synthesis of Ag_2MoO_4/BiOCl Heterojunction

To prepare the heterojunction, 0.15 g of BiOCl-OVs was dispersed in 50 mL of deionized water and subjected to sonication for 30 min. After that, 0.006 g of $AgNO_3$ was introduced into the above dispersion, followed by another 40 min of sonication. Subsequently, 0.012 g of $Na_2MoO_4{\cdot}2H_2O$ was added to the mixture, which was then stirred at room temperature for 1 h. The resulting product was collected by washing with deionized water and absolute ethanol, and then dried in an oven at 80 °C for 24 h. A series of composites with Ag_2MoO_4 to BiOCl-OVs mass ratios of 1%, 3%, 5%, 10%, and 15% were prepared and denoted as AB-1, AB-3, AB-5, AB-10, and AB-15, respectively. For comparison, pristine Ag_2MoO_4 was synthesized following the same procedure except that BiOCl-OVs were omitted.

2.4. Characterization

Powder X-ray diffraction (XRD, Billerica, MA, USA) patterns were recorded on a Bruker D8-Advance diffractometer equipped with Cu Kα radiation (λ = 0.15406 nm), operated at 40 kV and 40 mA with a scanning rate of 10°/min. X-ray photoelectron spectroscopy (XPS, Waltham, MA, USA) measurements were conducted on an ESCALAB 250Xi instrument to examine the surface chemical states and binding energies of the as-prepared composites. Morphological features and elemental compositions were characterized using field emission scanning electron microscopy (FESEM, SU8100, Tokyo, Japan) and high-resolution transmission electron microscopy (HRTEM, JEM-2100, Tokyo, Japan). Nitrogen adsorption–desorption isotherms were recorded on a BELSORP-mini II (Osaka, Japan) to determine the specific surface areas of the samples. UV-vis-NIR diffuse reflectance spectra (UV-vis DRS, Kyoto, Japan) were collected on a Shimadzu UV-3900 spectrophotometer (Japan) to evaluate light absorption properties. Photoluminescence (PL, Tokyo, Japan) spectra were acquired using a Hitachi F-4500 fluorescence spectrometer. Electrochemical and photoelectrochemical tests were performed on a CHI660E electrochemical workstation (Shanghai Chenhua, China) using a three-electrode quartz cell system with 0.5 M Na_2SO_4 as the electrolyte. Electron spin resonance (ESR, Billerica, MA, USA) spectra were recorded on a Bruker ER200-SRC spectrometer with DMPO as a spin-trapping agent in methanol and aqueous solutions.

2.5. Evaluation of Simulated Solar Driven Photocatalytic Performance

The photocatalytic activity of the Ag_2MoO_4/BiOCl heterojunction toward CIP degradation was tested at room temperature under a 350 W xenon lamp. Typically, 40 mL of an aqueous CIP solution (10 mg/L) containing 1 g/L of catalyst was magnetically stirred in the dark for 30 min to achieve adsorption–desorption equilibrium. Upon switching on the light, 3 mL samples were collected at designated time points and centrifuged. The remaining CIP concentration was analyzed using a UV-vis spectrophotometer (UV-2450).

3. Results and Discussion

3.1. Physicochemical Properties

The structure of BiOCl, Ag_2MoO_4 and a series of Ag_2MoO_4/BiOCl heterojunctions was studied by XRD. As shown in Figure 1a, the pure BiOCl exhibited distinct diffraction peaks at 2θ = 25.8°, 32.5°, 33.4°, 40.8°, 46.6°, 49.7°, 54.1° and 58.6°, corresponding to the (101), (110), (102), (112), (200), (113), (211) and (212) crystal planes of BiOCl (JCPDS No. 06-0249), respectively. Ag_2MoO_4 showed the characteristic diffraction peaks at 2θ = 27.1°, 31.8°, 33.3°, 38.6°, 50.1° and 55.8°, which were consistent with the diffraction peaks of Ag_2MoO_4 (JCPDS No. 08-0473). For Ag_2MoO_4/BiOCl heterojunction, the overall diffraction peak was consistent with that of tetragonal BiOCl. Obviously, when the loading amount of Ag_2MoO_4 exceeds 5%, a diffraction peak of Ag_2MoO_4 appears at 2θ = 33.3°, corresponding to the (222) crystal plane of Ag_2MoO_4. Furthermore, as the content of Ag_2MoO_4 increased, the diffraction peak gradually strengthened, indicating the formation of Ag_2MoO_4/BiOCl heterojunction. The nitrogen adsorption–desorption isotherms are presented in Figure 1b. BiOCl and AB-5 exhibited specific surface areas of 16.83 and 22.71 m^2/g, respectively. The increased specific surface area observed in AB-5 could be attributed to the fact that the Ag_2MoO_4 was deposited on the surface of BiOCl, forming a hierarchical structure.

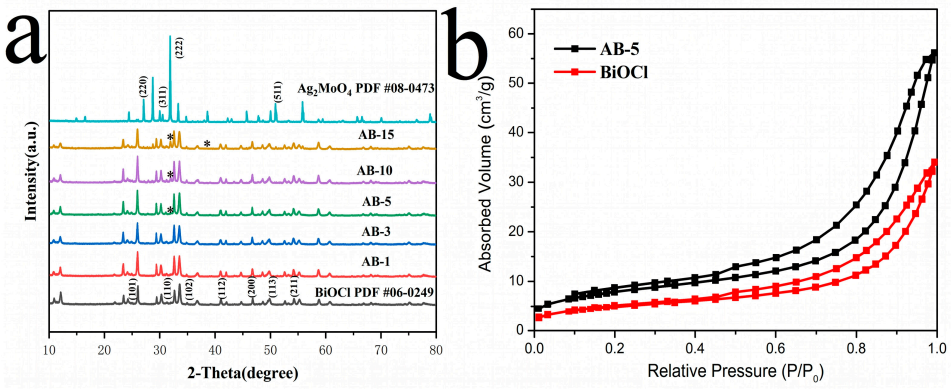


Figure 1. (**a**) XRD patterns of the standard diffraction card and (**b**) N_2 adsorption-desorption isotherms of as-synthesized samples.

In order to investigate the elements and chemical binding modes of the synthesized samples, XPS spectrum characterization was carried out. As shown in Figure 2a, the AB-5 heterojunction was mainly composed of five elements: Bi, O, Cl, Mo, and Ag. According to Figure 2b, the binding energies of Bi $4f_{7/2}$ and Bi $4f_{5/2}$ in AB-5 were 159.46 eV and 164.77 eV, respectively, indicating that the element Bi existed in trivalent form in the catalyst. As seen in Figure 2c, the binding energy at 530.34 eV indicates the presence of lattice oxygen in AB-5. The peaks at 531.52 and 532.08 eV were related to the O atoms near the OVs and surface O–H in the AB-5 heterostructure [40]. As seen in Figure 2d, the two characteristic peaks with binding energies of 198.22 eV and 199.82 eV are attributed to Cl $2p_{3/2}$ and Cl $2p_{1/2}$, corresponding to Cl^- in AB-5. Obviously, compared to pure BiOCl, Bi 4f, O 1s, and

Cl 2p in the AB-5 heterojunction moved towards lower binding energies. This might be due to the transfer of some electrons from Ag_2MoO_4 to BiOCl, resulting in an increase in electron density and a decrease in the binding energy of BiOCl [41,42]. As shown in Figure 2e, the Ag $3d_{5/2}$ and Ag $3d_{3/2}$ of AB-5 corresponded to binding energies of 367.90 eV and 373.91 eV, respectively. In Figure 2f, the peaks at 232.52 and 235.66 eV are ascribed to the Mo $3d_{5/2}$ and Mo $3d_{3/2}$ binding energy of Mo 3d, respectively. By comparison, it could be seen that the binding energies of Bi 4f, O 1s, Cl 2p, Ag 3d, and Mo 3d in the AB-5 heterojunction showed significant shifts, attributed to the interaction between Ag_2MoO_4 and BiOCl.

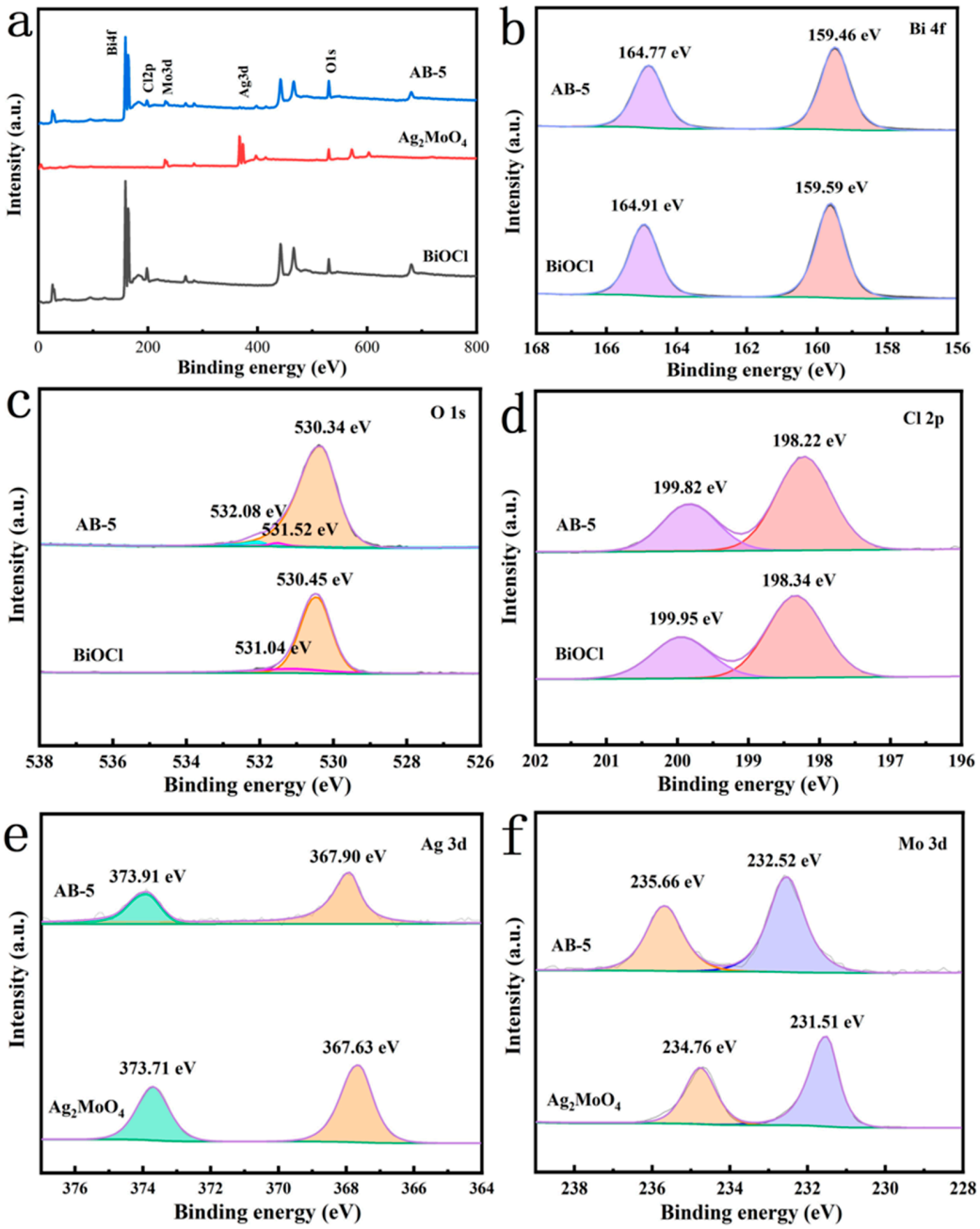


Figure 2. XPS spectra of Ag_2MoO_4, BiOCl, and AB-5 heterojunction: (**a**) survey XPS spectra (**b**) Bi 4f, (**c**) O 1s, (**d**) Cl 2p, (**e**) Ag 3d, (**f**) Mo 3d.

Figure 3 shows the SEM images of BiOCl, Ag_2MoO_4, and Ag_2MoO_4/BiOCl heterojunction. In Figure 3a, the pure BiOCl exhibited a smooth surface nanosheet with a diameter of 200–500 nm. As shown in Figure 3b, pure Ag_2MoO_4 showed a cubic crystal structure with a diameter of around 1–2 μm. The Ag_2MoO_4/BiOCl heterojunction (Figure 3c) showed that

the Ag_2MoO_4 particle was surrounded by sheet-like BiOCl, confirming that Ag_2MoO_4 and BiOCl had good interfacial contact, which was conducive to interfacial reactions. A possible reason for this phenomenon was that the Ag_2MoO_4 particles experienced a "dissolution–crystallization" mechanism during the reaction process, and the formed BiOCl nanosheets prevented the continuous growth of Ag_2MoO_4 grains due to a reduction in the surface energy.

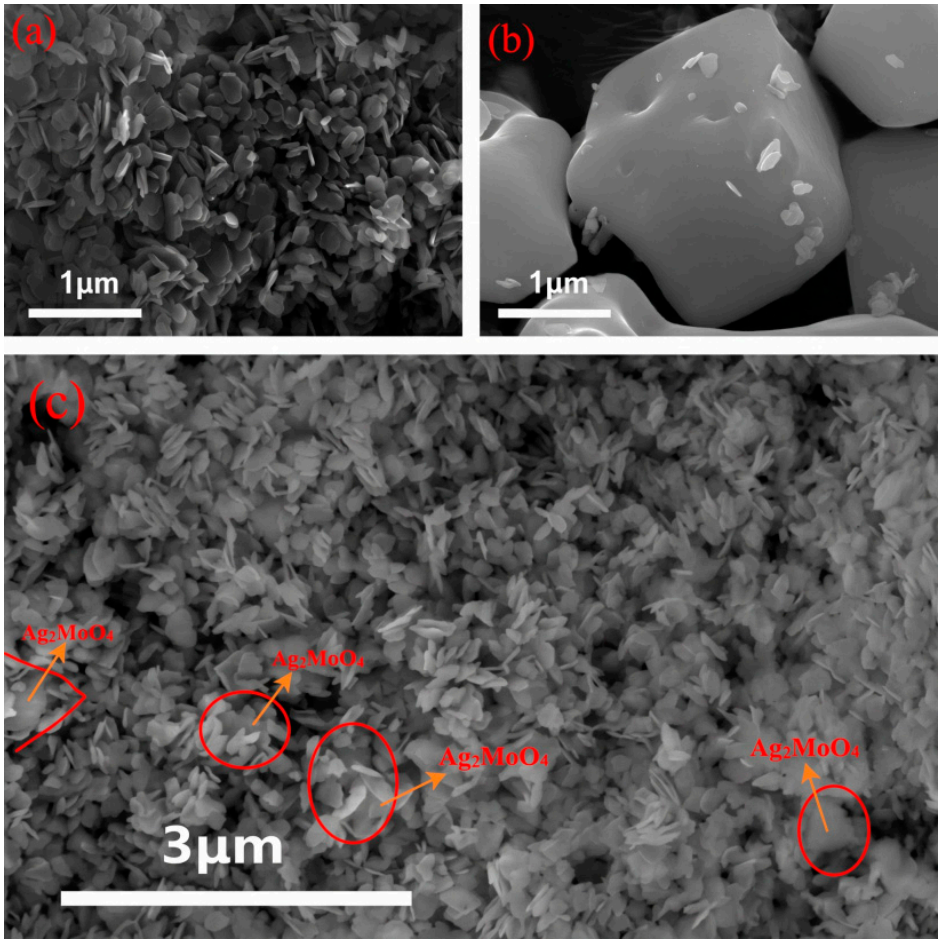


Figure 3. SEM of (**a**) BiOCl, (**b**) Ag_2MoO_4 and (**c**) AB-5 heterojunction.

Further examination of the AB-5 heterojunction was conducted using TEM and HRTEM. As illustrated in Figure 4a, Ag_2MoO_4 nanoparticles were deposited onto the two-dimensional BiOCl nanosheet surface. Figure 4b displays the lattice spacings of 0.34 nm and 0.32 nm, which correspond to the (101) plane of BiOCl and the (220) plane of Ag_2MoO_4, respectively. This provided additional evidence for the successful synthesis of the Ag_2MoO_4/BiOCl heterojunction.

The optical absorption property of the sample was studied using the UV–vis DRS analysis [43]. As shown in Figure 5a, the prepared photocatalyst exhibited significant absorption in both the ultraviolet and visible-light regions, and the Ag_2MoO_4/BiOCl heterojunction had stronger light absorption ability than pure BiOCl. The band gap could be calculated from the classic Tauc approach through the equation $\alpha h\nu = A(h\nu - E_g)^{n/2}$, where α, h, ν, A, and E_g are the optical absorption coefficient, Planck constant, photon frequency, a constant and band gap, respectively. According to the fitted band gap, the band gaps of BiOCl and Ag_2MoO_4 were estimated to be 3.25 eV and 3.36 eV, respectively (Figure 5b,c). Furthermore, Figure 6a,b reveals the valence band position of the as-prepared sample tested by VB-XPS spectra, suggesting that the VB positions of BiOCl and Ag_2MoO_4 were 3.42 and 3.11 eV, respectively. The CB

positions of BiOCl and Ag_2MoO_4 were calculated to be 0.17 eV and −0.25 eV, respectively, according to the energy band position formula $E_{CB} = E_{VB} - E_g$.

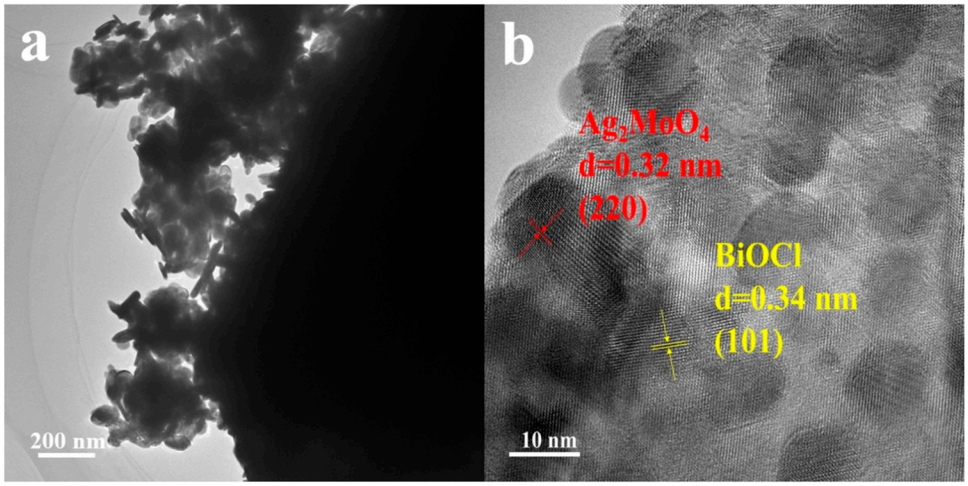


Figure 4. (**a**) The TEM and (**b**) HRTEM image of AB-5 heterojunction.

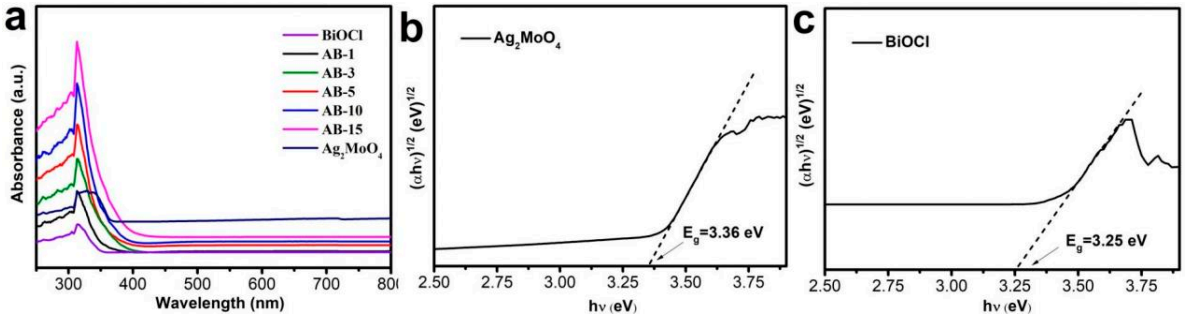


Figure 5. (**a**) UV-vis spectra and (**b**,**c**) band gap energies of Ag_2MoO_4 and BiOCl.

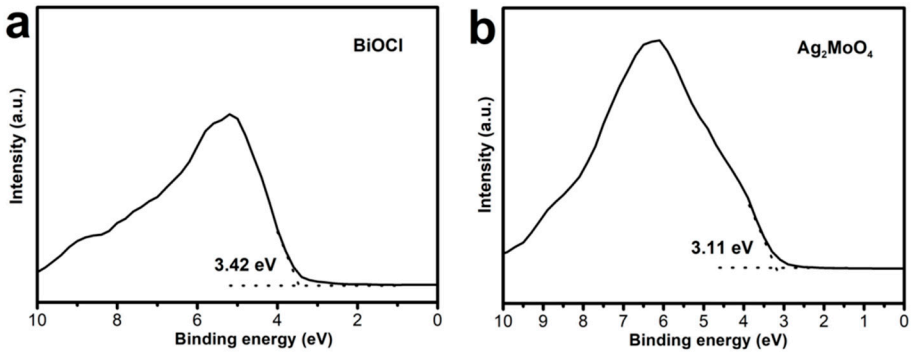


Figure 6. Valence-band XPS spectra of BiOCl (**a**) and Ag_2MoO_4 (**b**).

3.2. Photocatalytic Activity

The experiment employed ciprofloxacin (CIP) as a pollutant model to evaluate the photocatalytic activity of the synthesized samples. As depicted in Figure 7b, to ascertain the adsorption–desorption characteristics of the synthesized materials, a dark reaction was conducted for 180 min. The removal rate of AB-5 heterojunction remained essentially unchanged at both 30 min and 180 min, hence 30 min was chosen as the adsorption–desorption equilibrium point for this experiment. The control experiment indicated that CIP hardly degraded under simulated solar irradiation without the addition of a catalyst, suggesting that CIP was relatively stable. As seen in Figure 7a, the removal rates of CIP by

pure Ag_2MoO_4 and BiOCl photocatalysts were 24.60% and 42.25%, respectively. Under the same conditions, the AB-5 heterojunction exhibited the strongest photocatalytic activity, achieving a CIP degradation rate of 80.44% within 180 min. Furthermore, the degradation efficiency of the Ag_2MoO_4/BiOCl heterojunction first increased and then decreased with the increased content of Ag_2MoO_4, indicating that Ag_2MoO_4 played a crucial role in the photocatalytic degradation process. This was primarily due to the fact that the Ag_2MoO_4 helped enhance light absorption and promote the separation of photogenerated charge carriers. However, excessive Ag_2MoO_4 led to reduced photocatalytic activity. Similar loading-dependent behavior has recently been observed in BiOBr-based heterojunctions, where higher loadings of the secondary phase promoted growth along less reactive crystal facets and reduced the exposure of catalytically active surface sites, thereby diminishing charge separation efficiency [44]. The photocatalytic activity of the mechanically mixed Ag_2MoO_4/BiOCl composite was lower than that of the Ag_2MoO_4/BiOCl heterojunction, suggesting a better interfacial reaction between Ag_2MoO_4 and BiOCl. Due to the low initial concentration of CIP and fewer interfering factors in the initial stage, the photocatalytic reaction was modeled by the pseudo-first-order kinetics model, $ln\ (Co/C) = kt$, where Co and C were, respectively, the initial and instant concentrations at reaction time t, and k was the rate constant. As shown in Figure 7c, the k of the AB-5 heterojunctions were approximately 0.0119 min^{-1}, which was 2.76, 5.67, 1.71, 1.01, 1.33, and 1.13 times that of pure BiOCl, Ag_2MoO_4, AB-1, AB-3, AB-10, and AB-15 heterojunction. Figure 7d illustrates the absorbance spectrum of CIP following its degradation by the AB-5 heterojunction. It was evident that the characteristic absorption peak of CIP at 273 nm progressively diminished, signifying the gradual degradation of CIP.

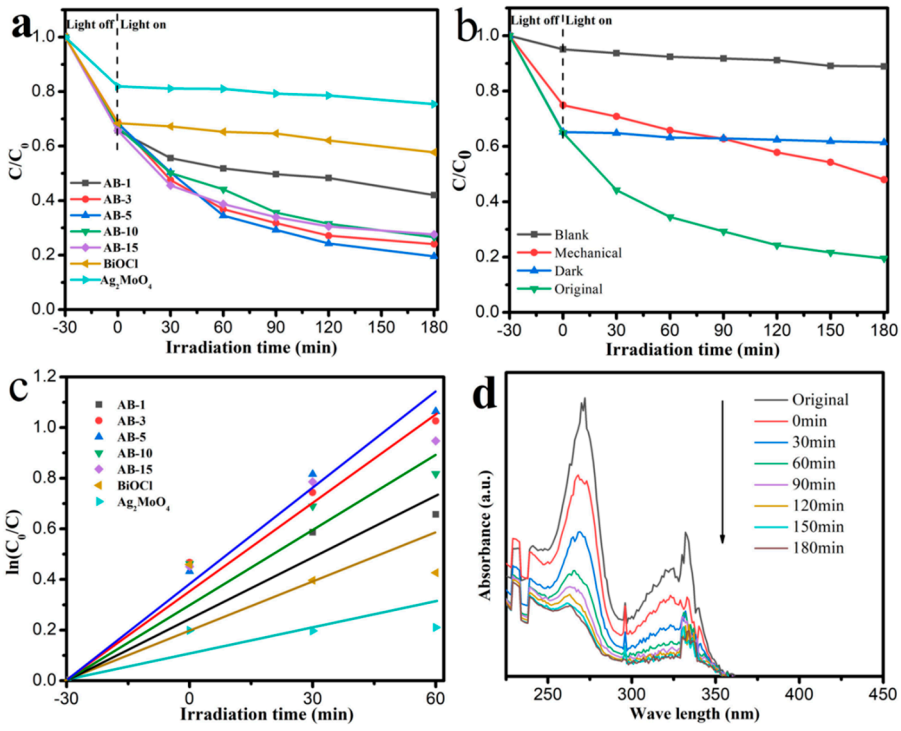


Figure 7. (**a**,**b**) Degradation efficiencies, (**c**) kinetic curves of CIP and (**d**) time-dependent absorption spectra of CIP with the as-prepared photocatalysts.

The experiment investigated the effect of catalyst usage on the degradation rate of CIP. As shown in Figure 8a, the results indicated that the photocatalytic degradation rate of CIP showed a significant improvement trend with the increase in AB-5 heterojunction dosage. When the dosage of AB-5 gradually increased from 20 mg to 40 mg, the removal

rate of CIP increased from 51.53% to 80.44%. This indicated that increasing the amount of photocatalyst could effectively improve the photocatalytic efficiency, as the addition of photocatalyst could generate more active species and accelerate the degradation of CIP [45]. However, when the dosage of photocatalyst continued to increase to 50 mg, the improvement in CIP degradation rate was no longer significant, indicating the existence of an optimal dosage of photocatalyst. Beyond this dosage, the photocatalyst did not bring higher photocatalytic efficiency, but instead increased costs. Therefore, in order to balance economy and efficiency, 40 mg was chosen as the optimal dosage for subsequent experimental research.

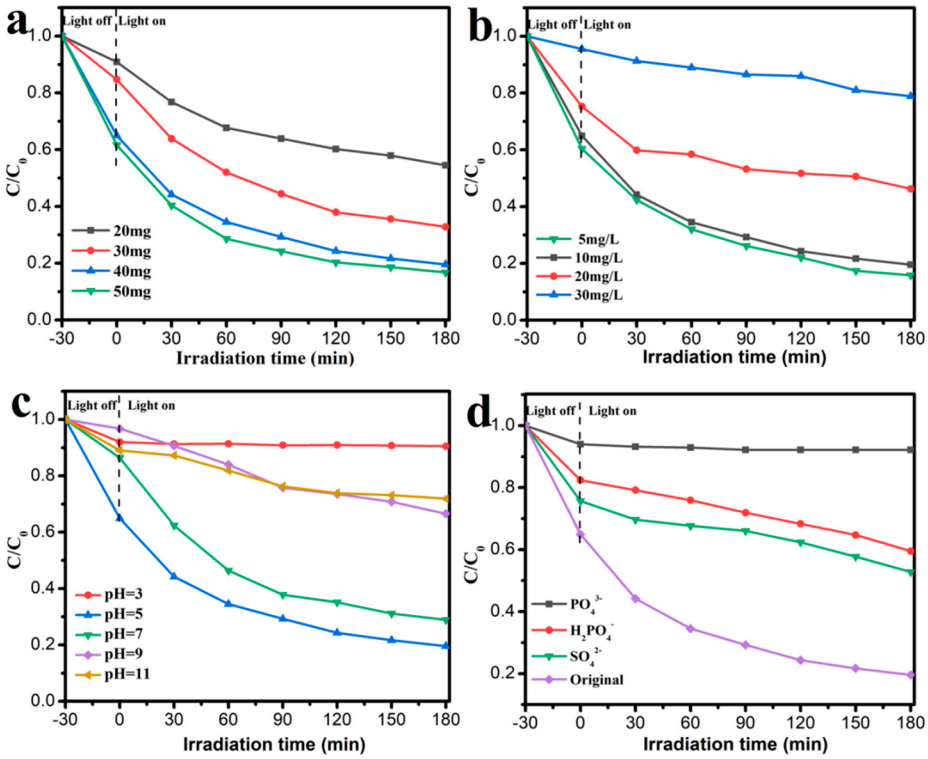


Figure 8. Degradation efficiencies of the CIP solution by (**a**) various AB-5 dosage ([CIP] = 10 mg/L), (**b**) various concentration of CIP ([AB-5] = 1 g/L), (**c**) at different pH, and (**d**) under different concentration of PO_4^{3-}, SO_4^{2-}, and $H_2PO_4^-$.

The experiment further investigated the effect of different CIP concentrations on the degradation efficiency. When the catalyst concentration was fixed at 1 g/L, the degradation rate of AB-5 under different CIP concentrations was explored by adjusting the initial concentration of CIP. As shown in Figure 8b, when the initial concentration of CIP was 5 mg/L, the photocatalytic degradation rate was the highest, reaching 84.17%. When the CIP concentration increased to 30 mg/L, the photocatalytic degradation rate significantly decreased to 21.12%. This phenomenon might be due to the rapid consumption of active species generated by photocatalyst AB-5 under high concentration CIP conditions, while high concentration CIP might also hinder the absorption of visible light, thereby reducing photocatalytic efficiency.

Figure 8c presents the influence of pH on the photocatalytic performance of the freshly prepared materials. The surface charge of CIP was significantly influenced by the pH of solution due to protonation and deprotonation reactions. When the pH was below 6.09, CIP tended to exist in a cationic form. Conversely, within the pH range of 6.09 to 8.62, CIP remained neutral [46]. When the pH decreased, it triggered electrostatic repulsion between the positively charged surface and the protonated CIP molecules, thereby diminishing

the adsorption of CIP onto the AB-5 heterostructure and resulting in reduced degradation efficiencies. Consequently, as the pH shifted from 5 down to 3, the degradation efficiencies of CIP exhibited the following ranking: pH 5 > pH 3. At pH 5, the AB-5 heterojunction exhibited the utmost degradation efficiency for CIP. Under neutral and alkaline conditions, as the alkalinity increased, the degradation efficiency of CIP gradually decreased.

In actual water environments, there were many other anion interferences. In order to simulate the actual water environment, the experiment was carried out by adding 1 mmol of sulfate ions (SO_4^{2-}), phosphate ions (PO_4^{3-}), and dihydrogen phosphate ions ($H_2PO_4^-$) to the solution of CIP to investigate the photocatalytic activity. As shown in Figure 8d, the degradation of CIP was inhibited to varying degrees after the addition of ions. Among them, the inhibitory effect of PO_4^{3-} was the most significant, with a removal rate of 7.81%. A possible reason was that PO_4^{3-} participated in the photocatalytic reaction process and reacted with the generated holes, thereby reducing the number of effective carriers involved in the degradation of ciprofloxacin. After the addition of $H_2PO_4^-$, the removal rate of CIP decreased to 40.48%, indicating that $H_2PO_4^-$ had a certain impact on the degradation of CIP. A possible reason was that $H_2PO_4^-$ reacted with the generated holes. The inhibitory effect of SO_4^{2-} was relatively weak, and the removal rate of CIP was 47.22%. This was mainly due to the capture of hydroxyl radicals and photogenerated holes by SO_4^{2-}, which reduced the activity of the catalyst [47].

In the study of the photocatalytic activity of Ag_2MoO_4/BiOCl heterojunction, it was considered that there may be multiple pollutants coexisting in actual water environments. As shown in Figure 9a–c, when LR5B and RhB coexisted with CIP, the degradation of CIP was significantly inhibited, with removal rates of 52.80% and 34.54%, respectively. This might be due to the competition between organic pollutants and active species. Simultaneously, a representative group of organic pollutants was selected for the experiment to test the degradation ability of AB-5 heterojunction, including tetracycline hydrochloride (TC), Lanasol Red 5B (LR5B) and rhodamine B (RhB), safranin T (SAT), and methyl orange (MO). As shown in Figure 9d, the Ag_2MoO_4/BiOCl heterojunction exhibited significant photocatalytic activity towards organic pollutants. The removal rate of LR5B and SAT reached 100% in 90 min, indicating that the heterojunction had the ability to completely mineralize the two types of organic pollutants. The removal rate of TC reached 60.24%, demonstrating excellent removal ability. The removal rate of RhB reached 51.74%, indicating good removal ability for the organic pollutant. However, for methyl orange, the removal rate was only 12.37%, indicating that the MO might have higher stability.

This trend could be explained by considering the molecular structures, functional groups, and electrostatic interactions with the AB-5 heterojunction surface. LR5B was an anionic reactive azo dye containing sulfonate groups (–SO_3^-), which strongly adsorbed onto the positively charged surface sites of AB-5 at pH 6.8, facilitating efficient electron transfer from the catalyst to the azo bonds (–N=N–) that were readily cleaved by photogenerated electrons and •O_2^-. SAT was a cationic phenazine dye with a planar aromatic structure that strongly adsorbed onto the negatively charged BiOCl surface via π-π stacking and electrostatic attraction, and its electron-rich aromatic rings were highly susceptible to attack by h^+ and •OH. CIP was a zwitterionic fluoroquinolone antibiotic with a piperazine ring and fluorine substituent. The degradation was efficient but slower than the dyes because the piperazine ring required multiple oxidation steps, and the fluorine atom stabilized the molecule. TC was a polyketide antibiotic with multiple phenolic and enolic hydroxyl groups that can chelate surface Bi^{3+} ions, but its larger molecular size and complex structure required sequential ring-opening steps, resulting in moderate degradation. RhB was a cationic xanthene dye with a bulky structure and ethylamino groups, which was limited by steric hindrance and the stability of the xanthene core, requiring extensive oxidation for

complete decolorization and mineralization. MO was an anionic azo dye with a dimethylamino group and a naphthalene ring. The poor degradation (12.37%) was attributed to the strong electron-withdrawing sulfonate group that reduces electron density on the azo bond [48].

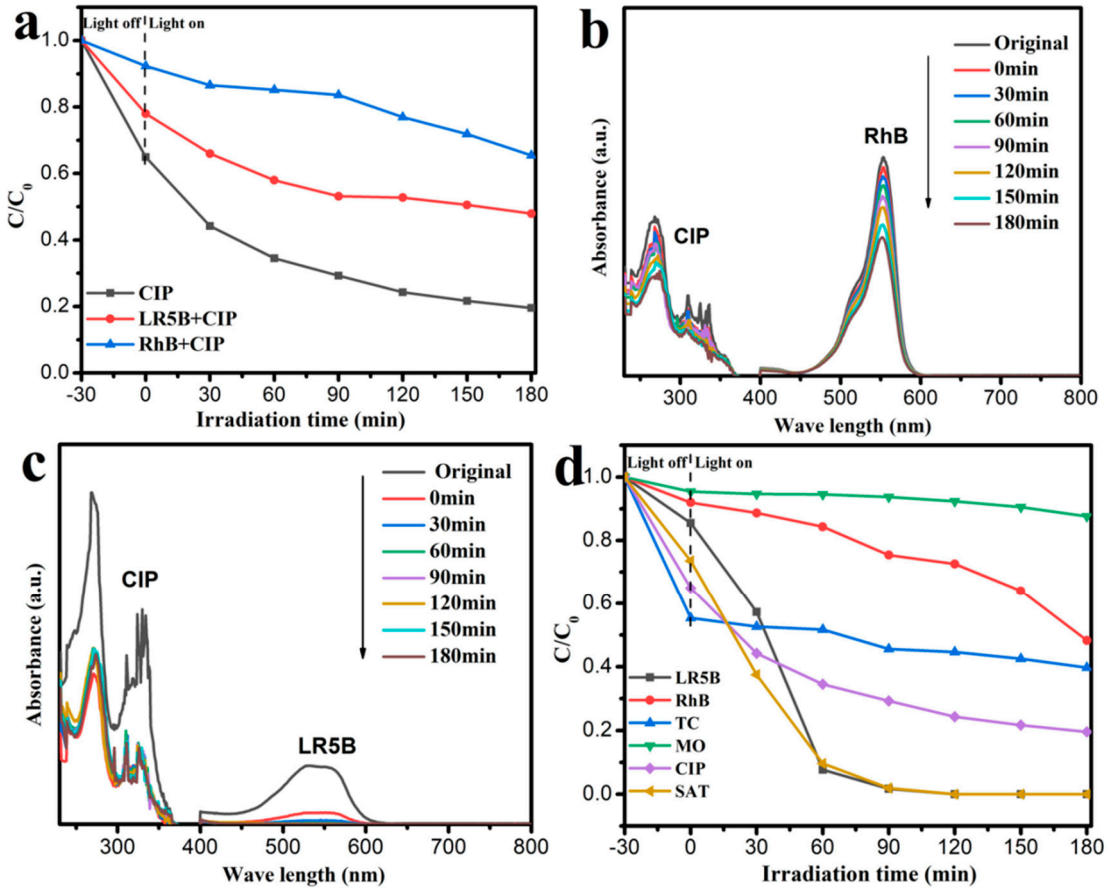


Figure 9. (**a**) Degradation efficiencies of CIP coexisting other pollutants, (**b**,**c**) time-dependent absorption spectra of organic substances degradation, (**d**) degradation efficiency of various pollutants in the presence of AB-5.

3.3. Photocatalytic Mechanism

PL spectroscopy was employed to study the recombination efficiency of photo-induced electrons and holes [49]. As shown in Figure 10a, all prepared materials exhibited a broad emission peak around 471 nm. Notably, AB-5 demonstrated the weakest PL intensity, indicating an improved charge separation efficiency, which could generate more reactive species, further enhancing its photocatalytic performance. In order to investigate the separation of photogenerated electron hole pairs in the AB-5 heterojunction, electrochemical experiments were conducted. As shown in Figure 10b, the AB-5 heterojunction exhibited a stronger photocurrent signal, indicating that the synergistic effect of oxygen vacancies and heterojunction could achieve lower recombination rates and faster charge transfer. Figure 10c shows the EIS curve of the sample. The smaller the impedance arc radius of the curve, the lower the charge transfer resistance on the electrode surface [50]. Comparing BiOCl and AB-5, AB-5 possessed the smaller impedance arc radius in the EIS curve, indicating that the interface charge transfer resistance of AB-5 was lower, and the separation and transfer of photogenerated electron–hole pairs was more effective.

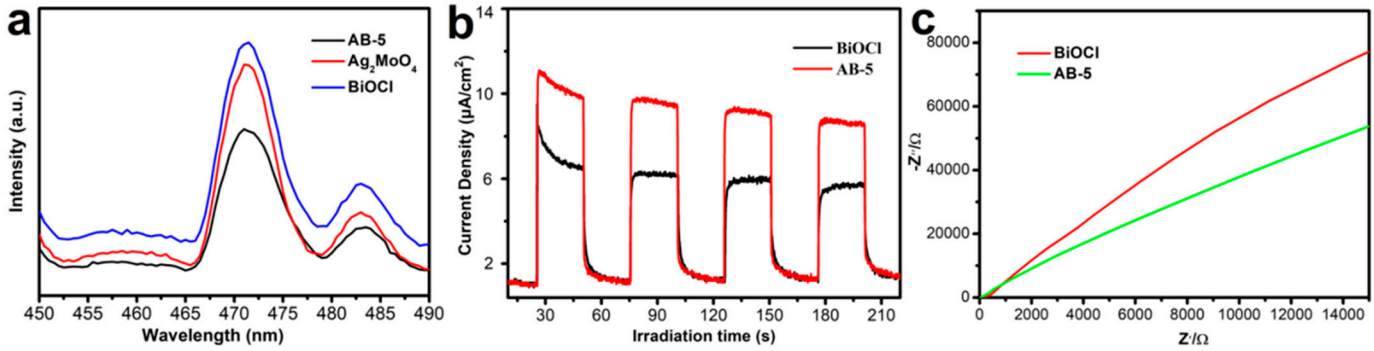


Figure 10. (**a**) PL spectra, (**b**) photocurrent-time transient and (**c**) EIS curves of the samples.

To study the photocatalytic mechanism of the AB-5 heterojunction, isopropanol (IPA), disodium ethylenediaminetetraacetate (EDTA-2Na), and benzoquinone (BQ) were added to capture hydroxyl radicals (•OH), holes (h^+), and superoxide radicals ($\bullet O_2^-$), respectively. The dosage of these scavengers was 2 mM [51]. As shown in Figure 11a, after adding EDTA-2Na to the reaction, the degradation rate of CIP was only 10.05%, and the degradation process was severely inhibited. However, after adding IPA and BQ, respectively, the degradation rates of CIP were 42.13% and 30.16%, indicating that the degradation process was slightly inhibited. The results indicate that h^+ was the main active substance in this photocatalytic reaction, while •OH and $\bullet O_2^-$ both played an auxiliary role in degradation.

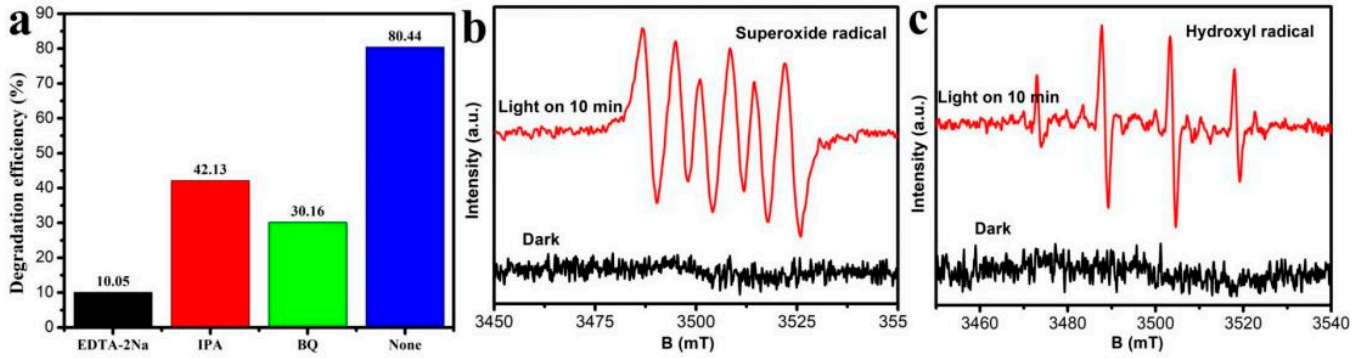


Figure 11. (**a**) Trapping experiments of active species during photodegradation of CIP in the presence of AB-5 heterojunction, (**b**) DMPO-$\bullet O_2^-$ and (**c**) DMPO-•OH adducts on AB-5 heterojunction.

ESR testing was used to demonstrate the presence of active free radicals in catalytic reactions. As shown in Figure 11b,c, no signals of DMPO-$\bullet O_2^-$ and DMPO-•OH were observed under dark conditions, indicating that $\bullet O_2^-$ and •OH were not generated in the absence of light. DMPO-$\bullet O_2^-$ and DMPO-•OH signals were detected after 10 min of simulated solar irradiation, which confirmed the production of $\bullet O_2^-$ and •OH in photocatalytic reactions. The ESR test results were basically consistent with the free radical capture experiment.

The possible charge transfer pathways of AB-5 heterojunction is shown in Figure 12. Firstly, if the AB-5 heterojunction belonged to the traditional Type II heterojunction, BiOCl and Ag_2MoO_4 became excited, causing photogenerated electrons to aggregate on the conduction band of BiOCl (Figure 12a). The photogenerated holes on the valence band of BiOCl eventually transferred to the valence band of Ag_2MoO_4, resulting in effective separation of photogenerated electrons and holes. However, the conduction band position of BiOCl was 0.17 eV, which was more positive than the standard redox potential of $E(O_2/\bullet O_2^-)$ (−0.046 eV vs. NHE) [52]. Consequently, if the heterojunction followed a traditional Type-II charge transfer pathway, the photogenerated electrons accumulating in

the CB of BiOCl (0.17 eV) would be unable to reduce O_2 to $\bullet O_2^-$ because this potential was more positive than $E(O_2/\bullet O_2^-) = -0.046$ eV. However, our trapping experiments clearly showed that $\bullet O_2^-$ was indeed generated and contributed to the degradation (30.16% inhibition with BQ), which contradicted the Type-II model and instead supported a Z-scheme mechanism, wherein electrons accumulated on the more negative CB of Ag_2MoO_4 (−0.25 eV) to produce $\bullet O_2^-$. Based on the above analysis, the Z-scheme heterojunction photocatalytic mechanism was adopted to explain the transfer path of photogenerated carriers in the AB-5 heterojunction. As shown in Figure 12b, BiOCl and Ag_2MoO_4 were excited, and electrons located in the conduction band of BiOCl transferred to the valence band of Ag_2MoO_4. Evidently, the holes located on the BiOCl valence band and the electrons on the Ag_2MoO_4 conduction band were effectively separated, exhibiting strong oxidizing and reducing properties, respectively. The valence band position of BiOCl was calculated to be 3.42 eV, which is higher than the standard oxidation–reduction potential of $E(\bullet OH/H_2O)$ (+2.72 eV vs. NHE) [53], indicating that the holes generated by BiOCl could oxidize H_2O to generate •OH. At the same time, the conduction band position of Ag_2MoO_4 was calculated to be −0.25 eV, which was more negative than the standard oxidation–reduction potential of $E(O_2/\bullet O_2^-)$ (−0.046 eV vs. NHE). The generated •OH and $\bullet O_2^-$ could further directly oxidize organic pollutants, achieving the effect of purifying water bodies.

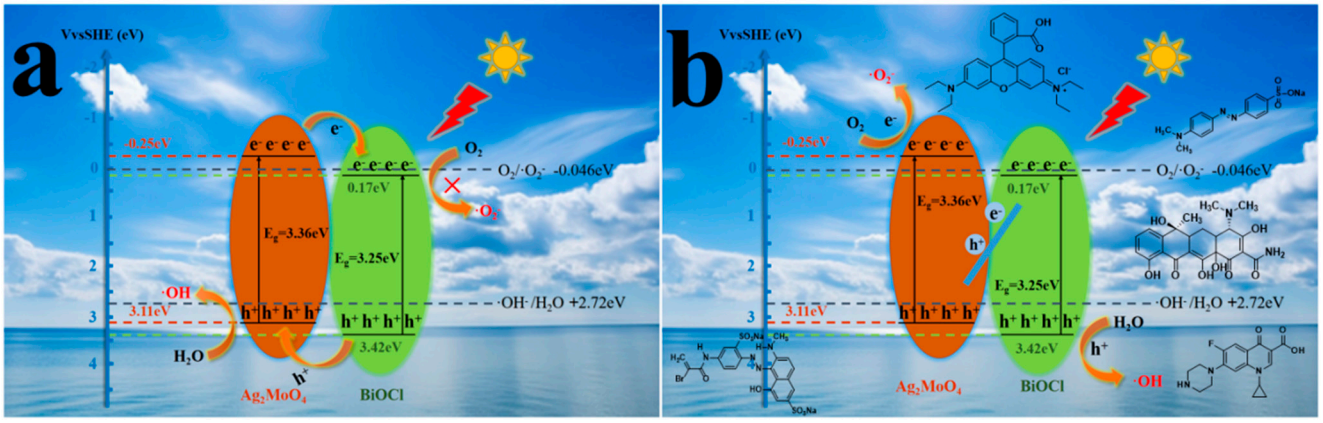


Figure 12. Proposed charge transfer and photocatalytic mechanisms for removal of CIP over the AB-5 heterojunction. (**a**) Schematic of the type-II heterojunction pathway, (**b**) Schematic of the proposed Z-scheme heterojunction pathway.

4. Conclusions

In summary, a novel Z-scheme Ag_2MoO_4/BiOCl heterojunction with oxygen vacancies was successfully prepared at a low temperature via a simple in situ precipitation method. The Ag_2MoO_4/BiOCl heterojunction exhibited efficient photocatalytic activity for various organic pollutants (LR5B (100%), SAT (100%), CIP (80.44%), TC (60.24%), RhB (51.74%), and MO (12.37%)) under simulated solar irradiation. When the loading amount of Ag_2MoO_4 was 5%, the Ag_2MoO_4/BiOCl heterojunction exhibited the best photocatalytic effect, with a degradation rate of 80.44% for CIP in 180 min, which was 1.90 times that of pure BiOCl. Environmental factor studies have shown that impurity ions (PO_4^{3-}, PO_4^{3-}) have a strong inhibitory effect on the photocatalytic reaction process. The results of the capture experiment and ESR indicated that h^+ played a crucial role in the photocatalytic degradation process, while $\bullet O_2^-$ and hydroxyl radicals •OH played auxiliary roles. As a novel photocatalyst, the Ag_2MoO_4/BiOCl heterojunction exhibited excellent performance in treating antibiotic containing wastewater and other recalcitrant organic pollutants, which was expected to provide an efficient and environmentally friendly new strategy for solving water pollution problems.

Author Contributions: S.F.: Conceptualization, Methodology, Software, Investigation, Formal analysis, Writing—original draft, Writing—review and editing. W.P.: Software, Resources. Q.H.: Conceptualization. H.Z.: Methodology, Software, Writing—review and editing. J.B.: Investigation, Formal analysis. Q.L.: Investigation, Data curation, Funding acquisition. B.Z.: Investigation. Z.Z.: Investigation, Software. Y.W.: Conceptualization, Visualization. H.W.: Formal analysis, Funding acquisition. All authors have read and agreed to the published version of the manuscript.

Funding: This research was funded by the National Nature Science Foundation of China grant number No. 12402430 and the Key research and development Project of Henan province No. 221111321500, the Natural Science Foundation of Henan No. 242300420350 and the 2025 Henan Housing & Urban-Rural Development S&T Project No. HNJS-2025-K24.

Institutional Review Board Statement: Not applicable.

Informed Consent Statement: Not applicable.

Data Availability Statement: All data, models, and code generated or used during the study appear in the submitted article.

Conflicts of Interest: The authors declare that they have no known competing financial interests or personal relationships that could have appeared to influence the work reported in this paper.

References

1. Mann, A.; Nehra, K.; Rana, J.; Dahiya, T. Antibiotic resistance in agriculture: Perspectives on upcoming strategies to overcome upsurge in resistance. *Curr. Res. Microb. Sci.* **2021**, *2*, 100030. [CrossRef] [PubMed]
2. Wang, K.; Zhuang, T.; Su, Z.; Chi, M.; Wang, H. Antibiotic residues in wastewaters from sewage treatment plants and pharmaceutical industries: Occurrence, removal and environmental impacts. *Sci. Total Environ.* **2021**, *788*, 147811. [CrossRef] [PubMed]
3. Girijan, S.K.; Paul, R.; Rejish Kumar, V.J.; Pillai, D. Investigating the impact of hospital antibiotic usage on aquatic environment and aquaculture systems: A molecular study of quinolone resistance in *Escherichia coli*. *Sci. Total Environ.* **2020**, *748*, 141538. [CrossRef] [PubMed]
4. Li, C.; Sun, Z.; Zhang, W.; Yu, C.; Zheng, S. Highly efficient g-C_3N_4/TiO_2/kaolinite composite with novel three-dimensional structure and enhanced visible light responding ability towards ciprofloxacin and *S. aureus*. *Appl. Catal. B-Environ.* **2018**, *220*, 272–282.
5. Qi, Z.; Wu, X.; Li, Q.; Lu, C.; Carabineiro, S.A.C.; Zhao, Z.; Liu, Y.; Lv, K. Singlet oxygen in environmental catalysis: Mechanisms, applications and future directions. *Coord. Chem. Rev.* **2025**, *529*, 216439. [CrossRef]
6. Sewon, O.; Erin, E.S. Recent advances in oxidative degradation of plastics. *Chem. Soc. Rev.* **2024**, *53*, 7309–7327. [CrossRef]
7. Trapasso, G.; Aricò, F. Organic carbonates as green media: From laboratory syntheses to industrial applications. *Green Chem.* **2025**, *27*, 6925–6966. [CrossRef]
8. Shi, X.M.; Kawai, K.; Okubo, M.; Yamada, A. Sequential structural evolution triggered by O–O dimerization in oxygen-redox reactions. *Adv. Energy Mater.* **2025**, *15*, 2405714.
9. So, M.; Yano, T.; Permatasari, A.; Nguyen, V.L.; Inoue, G. Role of pressure and expansion on the degradation in soli-state silicon batteries: Implementing electrochemistry in particle dynamics. *Adv. Funct. Mater.* **2025**, *35*, 2423877.
10. Parrino, F.; Gottuso, A.; Viganò, L.; Mariani, P.; Villa, I.; Cova, F.; Callone, E.; Dirè, S.; Palmisano, L.; Stredansky, M.; et al. Singlet oxygen photocatalytic generation by silanized TiO_2 nanoparticles. *Angew. Chem. Int. Ed.* **2024**, *8*, 1433–7851.
11. Fei, H.; Wu, J.; Zhang, J.; Zhao, T.; Guo, W.; Wang, X.; Yang, S.; Liu, G. Photocatalytic performance and its internal relationship with hydration and carbonation of photocatalytic concrete: A review. *J. Build. Eng.* **2024**, *97*, 110782. [CrossRef]
12. Sun, Z.L.; Yang, X.L.; Yu, X.F.; Xia, L.H.; Peng, Y.H.; Li, Z.; Zhang, Y.; Cheng, J.B.; Zhang, K.S.; Yu, J.Q. Surface oxygen vacancies of Pd/Bi_2MoO_{6-x} acts as "Electron Bridge" to promote photocatalytic selective oxidation of alcohol. *Appl. Catal. B Environ.* **2021**, *285*, 119790. [CrossRef]
13. Li, X.; Wan, Y.; Xie, Y.; Fu, Y.; Deng, F.; Zhou, Y.; Luo, Y.; Han, L.; Ma, J.; Dong, F.; et al. Synergistic Atomic-Vacancy Engineering in $Bi_2S_{3-\delta}$/Co-N-C: Boosting Photoelectrocatalytic Hydrogen Production via Formaldehyde Oxidation. *Adv. Funct. Mater.* **2025**, *36*, e23047. [CrossRef]
14. Kottarathil, S.; Abhinand, O.V.; Sridharan, K. In-situ engineered $KBiFe_2O_5$/BiOBr Z-scheme heterojunction photocatalyst for the pharmaceutical pollutant degradation and nitrogen fixation. *Appl. Surf. Sci.* **2026**, *718*, 164869. [CrossRef]

15. Johnson, E.; Raj, A.; Kottarathil, S.; Johansson, A.; Sridharan, K. Bismuth-rich $Bi_4O_5Br_2$ anchored on g-C_3N_4 nanosheets: Enhanced visible-light performance for simultaneous photocatalytic degradation of emerging pollutants and spectroscopic insights. *Sep. Pur. Tech.* **2025**, *364*, 132521.
16. Zhang, L.; Li, Y.; Li, Q.; Fan, J.; Carabineiro, S.A.C.; Lv, K. Recent advances on Bismuth-based Photocatalysts: Strategies and mechanisms. *Chem. Eng. J.* **2021**, *419*, 129484. [CrossRef]
17. Peng, T.; Wang, Y.; Dong, C.-L.; Nga, T.; Wu, B.; Wang, Y.; Guan, Q.; Zhang, W.; Shen, S. BiOCl atomic layers with electrons enriched active sites exposed for efficient photocatalytic CO_2 overall splitting. *Nano-Micro Lett.* **2025**, *17*, 223. [CrossRef]
18. Fan, Z.; Zhang, S.; Cheng, S.; Feng, Z.; Lv, H.; Song, H. Investigation into the performance and mechanism of BiOX photocatalytic degradation of toluene under sunlight. *ACS Omega* **2025**, *10*, 15082–15095. [CrossRef] [PubMed]
19. Lu, Y.; Chen, L.; Zhang, C.; Yu, M.; Lv, K.; Li, X.; Xi, B. Construction of oxidation-reduction bifunctional nano-purifiers: S-scheme faceted heterojunction BiOCl(110) nanosheets/TiO_2(001) hollow nanocubes with abundant oxygen vacancies for balancing visible photocatalytic activity. *J. Environ. Chem. Eng.* **2024**, *12*, 111893.
20. Guan, C.; Hou, T.; Nie, W.; Zhang, Q.; Duan, L.; Zhao, X. Sn^{4+} doping enhanced inner electric field for photocatalytic performance promotion of BiOCl based nanoflowers. *Appl. Surf. Sci.* **2022**, *604*, 154498. [CrossRef]
21. Guan, C.; Hou, T.; Nie, W.; Zhang, Q.; Duan, L.; Zhao, X. Boosting visible light driven gas–solid phase photocatalytic reduction of CO_2 on BiOCl microspheres by enhanced carrier transportation through lattice structure modification. *Sep. Purif. Technol.* **2023**, *306*, 122654.
22. Ouyang, L.; Ng, M.; Zhou, Z.; Wu, H.; Tang, M.; Chen, S. Manipulating charge dynamics in carbon nitride by carbon dot doping for efficient photocatalysis. *Adv. Sci.* **2025**, *12*, 2417390. [CrossRef]
23. Sherryna, A.; Yahia Zerga, A.; Zakaria, Z.; Tahir, M.; Jusoh, M. Advances in the morphological design and dimensional approaches of layered double hydroxides for photocatalytic applications: A Critical Review. *Energy Fuels* **2025**, *39*, 4565–4609. [CrossRef]
24. Yusuf, T.L.; Orimolade, B.O.; Masekela, D.; Adegoke, K.A.; Modibane, K.D.; Makgato, S.S. BiOX(X=Cl, Br, I)-based S-scheme heterostructure photocatalysts for environmental remediation and energy conversion. *Mater. Today Sustain.* **2025**, *30*, 101115.
25. Meng, L.H.; Zhao, C.; Wang, T.Y.; Chu, H.Y.; Wang, C.C. Efficient ciprofloxacin removal over Z-scheme ZIF-67/V-$BiOIO_3$ heterojunctions: Insight into synergistic effect between adsorption and photocatalysis. *Sep. Pur. Tech.* **2023**, *313*, 123511.
26. Li, L.; Cai, J.; Yan, Y.; Zhao, F.; Zhou, J. Flower-like direct Z-scheme $WS_2/Bi_2O_2CO_3$ photocatalyst with enhanced photocatalytic activity. *J. Alloy Compd.* **2019**, *810*, 151872.
27. Chen, Z.; Chen, J. One-pot steam-assisted synthesis of BiOCl/TiO_2/Zn-in-modified Mg-Al LDHs catalyst and its photocatalytic degradation of methylene blue. *Catalysts* **2026**, *16*, 494.
28. Warmuth, L.; Ritschel, C.; Feldmann, C. Facet-, composition- and wavelength-dependent photocatalysis of Ag_2MoO_4. *RSC Adv.* **2020**, *10*, 18377–18383. [CrossRef] [PubMed]
29. Zhang, J.; Wang, J.; Zhu, Q.; Zhang, B.; Xu, H.; Duan, J.; Hou, B.; Feldmann, C. Fabrication of a novel AgBr/Ag_2MoO_4@$InVO_4$ composite with excellent visible light photocatalytic property for antibacterial use. *Nanomaterials* **2020**, *10*, 10081541. [PubMed]
30. Vinoth Kumar, J.; Karthik, R.; Chen, S.-M.; Muthuraj, V.; Karuppiah, C. Fabrication of potato-like silver molybdate microstructures for photocatalytic degradation of chronic toxicity ciprofloxacin and highly selective electrochemical detection of H_2O_2. *Sci. Rep.* **2016**, *6*, 34149. [CrossRef]
31. Wang, H.; Wang, Y.; Xu, A.; Yang, Q.; Tao, F.; Ma, M.; Song, Z.; Chen, X. Facile synthesis of a novel WO_3/Ag_2MoO_4 particles-on-plate staggered type II heterojunction with improved visible-light photocatalytic activity in removing environmental pollutants. *RSC Adv.* **2019**, *9*, 34804–34813. [PubMed]
32. Song, Y.; Xie, W.; Yang, C.; Wei, D.; Su, X.; Li, L.; Wang, L.; Wang, J. Humic acid-assisted synthesis of Ag/Ag_2MoO_4 and Ag/Ag_2WO_4 and their highly catalytic reduction of nitro- and azo-aromatics. *J. Mater. Res. Tech.* **2020**, *9*, 5774–5783.
33. Liu, J.; Han, Z.; Xu, X.; Song, S.; Wang, H.; Yang, W.; Han, J. Plasmon-enhanced Z-scheme Ag_2MoO_4/Ag/In_2S_3 photocatalyst: Performance, mechanism and application insights. *Mat. Sci. Eng. B-Adv.* **2026**, *324*, 119068.
34. Ni, H.; Zou, X.; Dong, Y.; Ke, J.; Ge, H.; Cui, Y. Z-scheme Ag_2MoO_4/g-C_3N_4 heterojunction photocatalysts for sulfadiazine degradation under sunlight irradiation. *J. Environ. Chem. Eng.* **2025**, *13*, 117945.
35. Wang, B.; Wang, C.; Tang, Y.; Yang, H.; Tian, Y.; Yu, X.; Li, Q. High-efficiency photodegradation of levofloxacin enabled by hybrid Ag_2MoO_4@AgCl composites: Performance, pathways, and mechanism insight. *Appl. Surf. Sci.* **2025**, *697*, 162970.
36. Jatav, N.; Kumar, U.; Shrivastava, A.; Singh, N.; Sinha, I. Fabrication of $Ag_2MoO_4/CuWO_4$ Nanocomposite Photocatalyst for the Degradation of Rhodamine-B. *ChemistrySelect* **2024**, *9*, e202400963. [CrossRef]
37. Fan, G.; Hu, K.; Xia, M.; Cai, C.; He, Z.; Luo, J.; Xu, K. Z-scheme $Ag_2MoO_4/BiVO_4$ photocatalyst using Ag as charge transfer mediator: Performance optimization and *Microcystis aeruginosa* inactivation application. *J. Environ. Chem. Eng.* **2024**, *12*, 111847. [CrossRef]
38. Wang, H.; Chen, S.; Zhu, X.; Liu, D.; Li, K.; Yuan, R.; Zhu, X. Construction of $Ag_2MoO_4/ZnWO_4$ S-scheme heterojunction photocatalytic composite materials and photocatalytic performance toward levofloxacin degradation. *Inorg. Chem. Commun.* **2026**, *190*, 116826.

39. Fu, S.; Chu, Z.; Huang, Z.; Dong, X.; Bie, J.; Yang, Z.; Zhu, H.; Pu, W.; Wu, W.; Liu, B. Construction of Z-scheme AgCl/BiOCl heterojunction with oxygen vacancies for improved pollutant degradation and bacterial inactivation. *RSC Adv.* **2024**, *14*, 3888. [PubMed]
40. Fu, S.; Yuan, W.; Liu, X.; Yan, Y.; Liu, H.; Li, L.; Zhao, F.; Zhou, J. A novel 0D/2D WS2/BiOBr heterostructure with rich oxygen vacancies for enhanced broad-spectrum photocatalytic performance. *J. Colloid Interface Sci.* **2020**, *569*, 150–163. [CrossRef] [PubMed]
41. Li, K.; Zhang, C.; Li, X.; Du, Y.; Yang, P.; Zhu, M. A nanostructured $CuWO_4/Mn_3O_4$ with p/n heterojunction as photoanode toward enhanced water oxidation. *Catal. Today* **2019**, *335*, 173–179.
42. Chen, F.; Li, D.; Luo, B.; Chen, M.; Shi, W. Two-dimensional heterojunction photocatalysts constructed by graphite-like C_3N_4 and Bi_2WO_6 nanosheets: Enhanced photocatalytic activities for water purification. *J. Alloys Compd.* **2017**, *694*, 193–200.
43. Ma, J.; Xu, L.; Yin, Z.; Li, Z.; Song, Z.; Qiu, J.; Li, Y. Boosting charge transfer of BiOBr/AgBr S-scheme heterojunctions via interface Br atom co-sharing for enhanced visible-light photocatalytic activity. *Green Energy Environ.* **2025**, *10*, 1073–1084. [CrossRef]
44. Giovilli, G.; Merlo, F.; Olivati, A.; Chems, M.; Speltini, A.; Loriso, M.; Colella, S.; Listorti, A.; Landi, A.; Peluso, A.; et al. Mechanistic insights into the nitrogen photofixation reaction by BiOBr-based heterojunctions. *J. Mater. Chem. C* **2026**, *14*, 5960–5969. [CrossRef]
45. Song, W.; Zhao, J.; Xie, X.; Liu, W.; Liu, S.; Chang, H.; Wang, C. Novel BiOBr by compositing low-cost biochar for efficient ciprofloxacin removal: The synergy of adsorption and photocatalysis on the degradation kinetics and mechanism insight. *RSC Adv.* **2021**, *11*, 15369–15379. [PubMed]
46. Fu, S.; Liu, X.; Yan, Y.; Li, L.; Liu, H.; Zhao, F.; Zhou, J. Few-layer WS2 modified BiOBr nanosheets with enhanced broad-spectrum photocatalytic activity towards various pollutants removal. *Sci. Total Environ.* **2019**, *694*, 133756. [PubMed]
47. Fu, S.; Zhu, H.; Huang, Q.; Liu, X.; Zhang, X.; Zhou, J. Construction of hierarchical $CuBi_2O_4$/Bi/BiOBr ternary heterojunction with Z-scheme mechanism for enhanced broad-spectrum photocatalytic activity. *J. Alloys Compoun.* **2021**, *878*, 160372.
48. Wang, Y.; Zhu, H.; He, P.; Li, M.; Cao, Y.; Du, Y.; Wen, Y.; Zhao, Y.; Liu, X.; Song, Y. Two-dimensional silver Bismuth Oxide/Bismuth Molybdate Z-Scheme Heterojunctions with Rich Oxygen Vacancies for Improved pollutant degradation and bacterial inactivation. *Crystals* **2025**, *15*, 318.
49. Cao, J.; Chen, X.; Chen, C.; Chen, A.; Zheng, W. High efficiency $Bi_2S_3/Bi_2MoO_6/TiO_2$ photoanode for photoelectrochemical hydrogen generation. *J. Alloy. Compd.* **2023**, *965*, 171139.
50. Nehru, B.S.; Perumal, N.; Subbarayalu, P.Y. Sustainable water treatment: Synthesis and characterization of g-$C_3N_5/NiCo_2S_4$ heterojunction nanocomposite for efficient visible light-induced degradation of highly hazardous organic pollutants. *J. Water Process Eng.* **2025**, *73*, 107712.
51. Zou, J.P.; Ma, J.; Luo, J.M.; Yu, J.; He, J.; Meng, Y.; Luo, Z.; Bao, S.K.; Liu, H.L.; Luo, S.L.; et al. Fabrication of novel heterostructured few layered WS_2-$Bi_2WO_6/Bi_{3.84}W_{0.16}O_{6.24}$ composites with enhanced photocatalytic performance. *Appl. Catal. B-Environ.* **2015**, *179*, 220–228.
52. Li, L.; Yan, Y.; Liu, H.; Du, J.; Fu, S.; Zhao, F.; Xu, S.-M.; Zhou, J. Hollow core/shell β-Bi_2O_3@WS_2 p–n heterojunction for efficient photocatalytic degradation of fluoroquinolones: A theoretical and experimental study. *Inorg. Chem. Front.* **2020**, *7*, 1374–1385.
53. Liu, H.; Liang, J.; Shao, L.; Du, J.; Gao, Q.; Fu, S.; Li, L.; Hu, M.; Zhao, F.; Zhou, J. Promoting charge separation in dual defect mediated Z-scheme MoS_2/gC_3N_4 photocatalysts for enhanced photocatalytic degradation activity: Synergistic effect insight. *Colloid Surf. A* **2020**, *594*, 124668. [CrossRef]

Disclaimer/Publisher's Note: The statements, opinions and data contained in all publications are solely those of the individual author(s) and contributor(s) and not of MDPI and/or the editor(s). MDPI and/or the editor(s) disclaim responsibility for any injury to people or property resulting from any ideas, methods, instructions or products referred to in the content.